Electronic Supplementary Material (ESI) for Soft Matter.

Supporting Information

"Lack of a unique kinetic pathway in the growth and decay of Pluronics micelles"

Alexandra Arranja,[†] Gilles Waton,[†] François Schosseler,[*,†] and Eduardo Mendes[‡]

Institut Charles Sadron, CNRS-University of Strasbourg, UPR 22, 23 rue du Loess, 67034 Strasbourg Cedex 2, France, and Delft University of Technology, Department of Chemical Engineering, Advanced Soft Matter, Julianalaan 136, 2628 BL, Delft, The Netherlands, EU.

E-mail: francois.schosseler@ics-cnrs.unistra.fr

[*]To whom correspondence should be addressed
[†]Institut Charles Sadron
[‡]TU Delft

Contents

I. Polymer characterization

1. Size exclusion chromatography and purification
2. ^{1}H-NMR
3. Micro Differential Scanning Calorimetry (MicroDSC)

II. Data analysis

1. CONTIN analysis
2. Analysis of $P(\tau_i)$ and parameter definitions
3. Automated peak identification and sorting
4. Other methods of analysis
5. Comparison of the methods of analysis

III. Crossover and polydispersity effects

1. Out of Guinier range
2. Polydispersity
3. To semidilute regime

IV. Specific results

1. Angular dependence of slow decay mode intensity for P84 at $T = 32, 33°$C
2. Angular dependence of slow decay mode for P94 at $T = 29, 30°$C
3. Angular dependence of fast and slow modes for P104 at $T = 34°$C

I. Polymer characterization

1. Size exclusion chromatography and purification

All block copolymers used in this study were characterized by Size Exclusion Chromatography (SEC). Samples were dissolved in HPLC quality tetrahydrofuran and the chromatograms were recorded using a differential refractive index detector (Shimadzu SPD 10Avp UV). The columns were filled with PLgel of four different porosities (50 Å, 100 Å, 500 Å, 1000 Å), and nine homopolymers of PEO (194 - 18380 g/mol) were used as standards for the calibration curve.

SEC analysis of commercial triblock copolymers revealed two main peaks (Fig. S1). The strong peak is attributed to the triblock copolymers, while the small peak corresponds to low molecular weight impurities. These copolymers are often used without purification despite the fact that previous studies have shown that the presence of impurities affects the dynamics of the raw copolymers.[1–4]

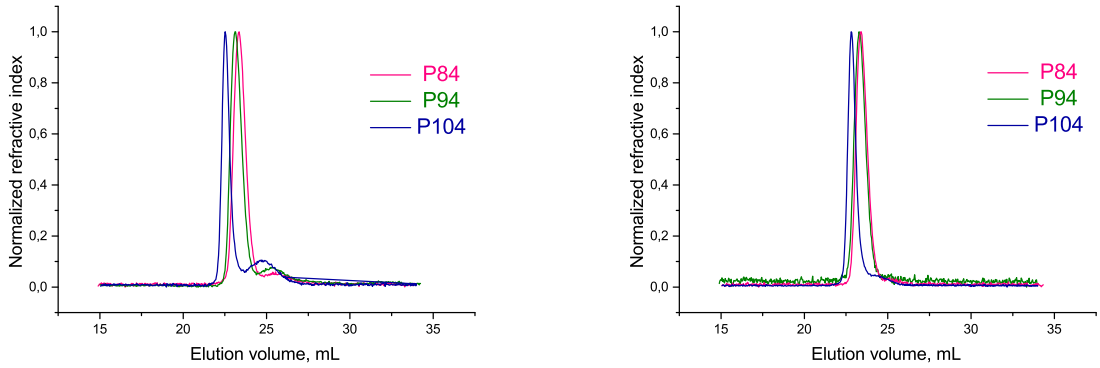

Figure S1: Size exclusion chromatograms of commercial P84, P94 and P104 samples analyzed as received (left) and after purification (right).

Table S1: Contents of low molecular weight impurities before and after purification (SEC analysis).

	Before purification			After purification		
sample	M_w	PDI[a]	%[b]	M_w	PDI[a]	%[b]
P84	4800	1.06	8	4800	1.06	0
P94	5200	1.05	15	5100	1.05	2
P104	8100	1.05	25	8000	1.05	7

[a] M_w/M_n for the main peak; [b] % (w/w) of low molecular weight impurities.

The low molecular weight impurities can be either smaller triblock copolymers, diblock copolymers (PEO-PPO) or homopolymers of PEO or PPO. Therefore, in order to avoid the use of unspecific methods in relation to the variety of contaminants that may be present and also to avoid the use of organic solvents, the samples were purified by dialysis. Concentrated aqueous solutions of the copolymers (10 wt%) were prepared and dialyzed against distilled water using regenerated cellulose membranes (cut-off 3.5 kDa, Roth). Dialysis was performed for 7 days, and the water was changed 4 times in the first three days, and then twice-daily. After purification, the water in the polymer solution was removed by vacuum drying, and the obtained products were analyzed by SEC (Fig. S1,

Table S1) and ^{1}H-NMR (see example on Fig. S2). Gravimetric analysis revealed that most of the water was removed by vacuum drying (water content $< 1\%$).

2. ^{1}H-NMR

2.1. Propylene oxyde/ethylene oxyde (PO/EO) ratio determination

The PO/EO ratio can be easily determined using ^{1}H-NMR. A small amount of Pluronic sample (5-10 mg) was dissolved in 1 mL of $CDCl_3$ and the ^{1}H-NMR recorded in a Bruker 400 Ultrashield. The PO units are characterized by a narrow signal at about 1.1 ppm (-CH3 group). The CH_2O/CHO units cause a multiplet between 3.2 and 3.8 ppm (Fig. S2). The % of EO was calculated using the following equations[5]

$$\%EO = \frac{3300\alpha}{33\alpha + 58} \tag{1}$$

$$\alpha = \frac{area(\mathrm{CH_2/CHO})}{area(\mathrm{CH_3})} - 1 \tag{2}$$

2.2. Determination of the number of repeating units

To determine the number of repeating units, the following equation was used[6]

$$n_x = \frac{a_x m_y n_y}{a_y m_x} \tag{3}$$

where

a_x = area of unknown sequence (PO or EO)

n_x = number of repeating units

m_x = number of protons

a_y = peak area of end group

n_y = number of repeating units

m_y = number of protons

The protons of the end groups (-OH) are not well discriminated in the ^{1}H-NMR because they arise in the same area as the signals from the non-terminal EO and PO groups. Thus, to determine

the area of the end group (a_y), the signal was displaced. For this, the polymers were reacted with trichloroacetyl isocyanate (TAIC, Sigma-Aldrich),[7] which readily reacts with terminal hydroxyl groups according to Scheme 1. Approximately 10 mg of purified sample were dissolved in 500 μL of $CDCl_3$, and 10 μL of TAIC were added at room temperature. The ^{1}H-NMR spectrum was recorded after $\approx$ 10 minutes to allow complete reaction. After the reaction with the displacement reagent, a new signal arises in the ^{1}H-NMR spectra at 4.4-4.5 ppm (see ^{1}H-NMR for Pluronic P94 in Fig. S2 before and after reaction with TAIC).

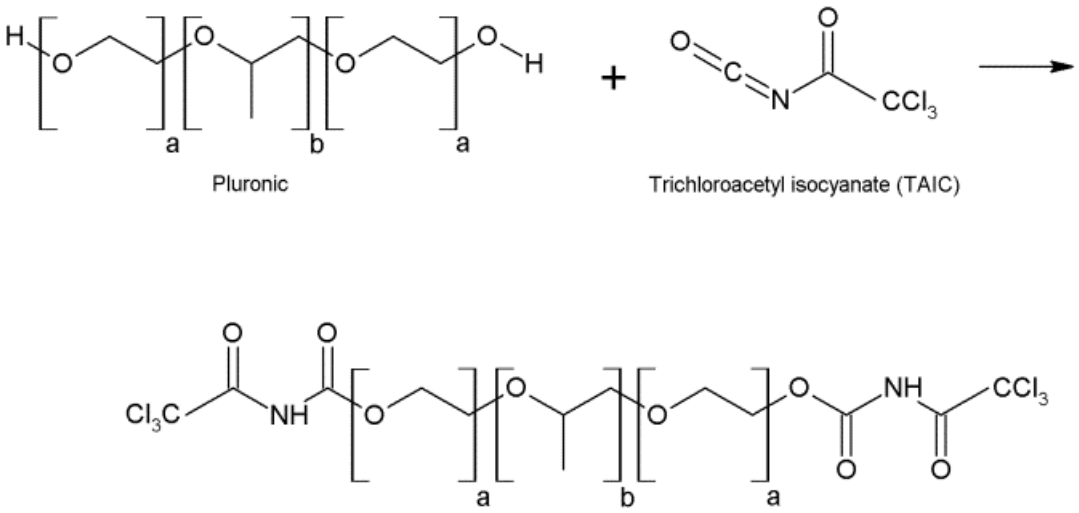

Scheme S1: Reaction between Pluronic and trichloroacetyl isocyanate.

2.3. Molecular weight determination

The total molecular weight was determined using the respective number of repeating units (n_{PPO} and n_{PEO}) determined before, the molecular mass of each unit, and the molecular mass of the end groups.

The results obtained from the ^{1}H-NMR are represented in Table S2 along with the information provided by the manufacturer. Similar results to ours were obtained before using ^{1}H and ^{13}C NMR for Pluronic P94[2] and MALDI-TOF MS for Pluronic P104[8] which also differ from the information provided by the manufacturer.

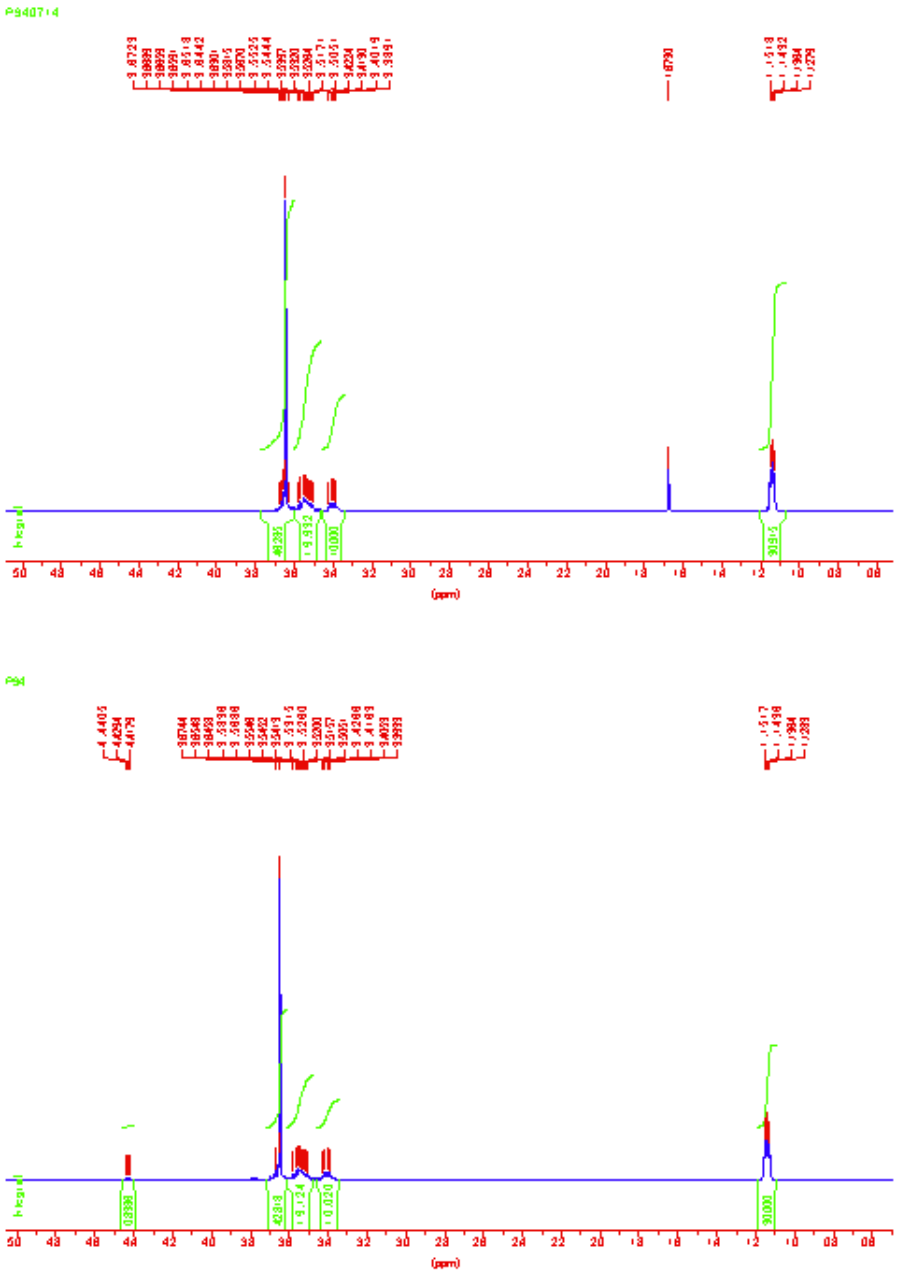

Figure S2: ^{1}H-NMR spectrum of purified Pluronic P94 before (above) and after reaction with displacement reagent (TAIC).

Table S2: Characteristics of purified samples.

PEO blocks

Samples	% PEO			n_{PEO}		M_w PEO	
	^{1}H-NMR		Supplier[a]	^{1}H-NMR[c]	Supplier[a]	^{1}H-NMR	Supplier[a]
	Without TAIC[b]	With TAIC[c]					
P84	44	43	40	46	38	2020	1670
P94	45	45	40	51	42	2240	1850
P104	39	39	40	56	53	2440	2350

PPO blocks

Samples	% PPO			n_{PPO}		M_w PPO	
	^{1}H-NMR		Supplier[a]	^{1}H-NMR[c]	Supplier[a]	^{1}H-NMR	Supplier[a]
	Without TAIC[b]	With TAIC[c]					
P84	56	57	60	46	43	2670	2510
P94	55	55	60	48	47	2770	2750
P104	61	61	60	66	61	3830	3530

Copolymers

	Total molecular weight		Formula	
Samples	^{1}H-NMR	Supplier[a]	^{1}H-NMR	Supplier[a]
P84	4700	4200	$EO_{23}PO_{46}EO_{23}$	$EO_{19}PO_{43}EO_{19}$
P94	5000	4600	$EO_{26}PO_{48}EO_{26}$	$EO_{21}PO_{47}EO_{21}$
P104	6300	5900	$EO_{28}PO_{66}EO_{28}$	$EO_{27}PO_{61}EO_{27}$

[a] Values provided by BASF; [b] PO/EO ratio determination (see equations in section 2.1);
[c] Number of repeating units (see equation in section 2.2).

3. Micro Differential Scanning Calorimetry (MicroDSC)

MicroDSC experiments were performed in a Micro DSC III Setaram calorimeter. Heating and cooling scans were used with heating and cooling rates of 0.2 and 0.1°C/min, respectively. The data were analyzed using SETSOFT 2000 (Setaram).

Fig. S3 presents the MicroDSC heating scans of 0.5% solution of Pluronic P84, P94 and P104 in 2M NaCl. The first and fairly broad peak is assigned to the aggregation of unimers into micelles (micellization). The CMT was determined after integration of the peaks and it decreases as the molecular weight increases as expected. The CMT values are 10, 9 and 2°C for Pluronic P84, P94 and P104, respectively.

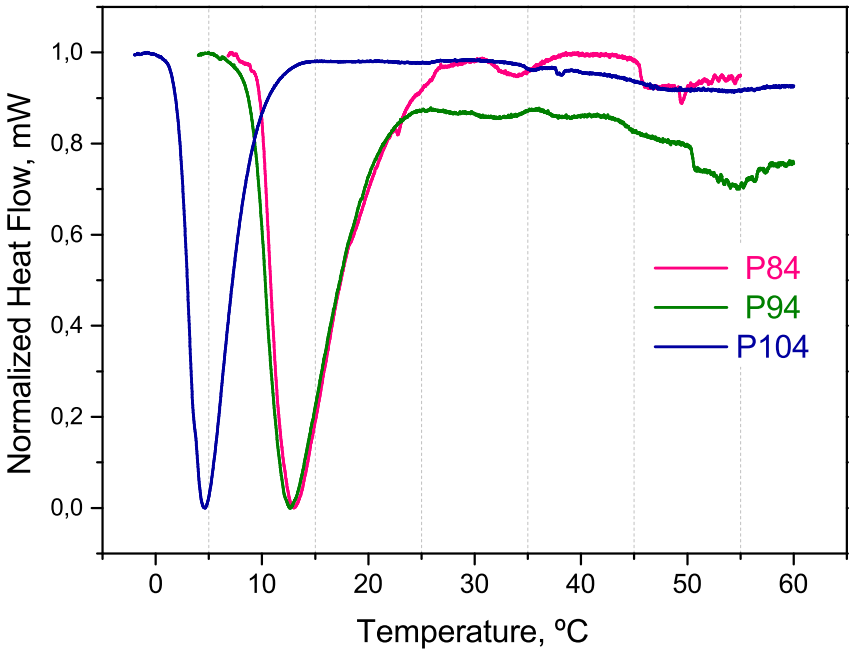

Figure S3: MicroDSC heating scans for the three copolymers.

The following transitions with much smaller amplitude are probably related to the sphere-to-rod transition. Different behaviors were observed with all the copolymers: with P84 we observed a small transition at around 31°C after micellization has ended, with P94 the micellization does not end and several steps of transition are observed, and with the P104 almost no transition was observed.

According to the slow kinetics of micellar growth observed in this paper, the MicroDSC technique

is not suitable for the micellar growth analyses. The heating scans lasted in general 5 hours, which is not enough time to observe the slow transitions. The last abrupt transition corresponds to the beginning of a phase separation process which is not complete at these temperatures, and does not start for the P104 copolymer.

II. Data analysis

All the analysis was done with a compiled version of the original FORTRAN-written CONTIN and with the help of home-written scripts that allow batch analysis of a large number of ICFs. These scripts are based on the previously described CNTb package[9] and allow a careful propagation of error estimations in the calculated quantities.

1. CONTIN analysis

For polydisperse systems with a distribution of relaxation time $p(\tau)$, the normalized intensity-intensity correlation function $g^{(2)}(t)$ is written as:[10]

$$g^{(2)}(t) = 1 + (\beta g^{(1)}(t))^2 = 1 + (\beta \int p(\tau) \exp(-t/\tau) d\tau)^2 \tag{4}$$

$$g^{(1)}(t) = \frac{< E(t'+t)E^*(t') >_{t'}}{< I(t') >_{t'}} \tag{5}$$

where $g^{(1)}(t)$ is the normalized autocorrelation function of the scattered electric field $E(t)$ and $\beta \leq 1$ is a numerical factor close to unity that depends on the geometry of detection. Formally, $g^{(1)}(t)$ is the Laplace transform of $p(\tau)$. Due to data noise, trying to numerically inverse Laplace transform of $g^{(1)}(t)$ to obtain $p(\tau)$ is not possible without very large numerical errors. A different approach has been proposed by S.W. Provencher[11] with the CONTIN method. In Eq. 4 $g^{(1)}(t)$ can be discretized as:

$$\beta g^{(1)}(t) = \widetilde{g}^{(1)}(t) = \sum_{i=1}^{N_g} P(\tau_i) \exp(-t/\tau_i) \tag{6}$$

where N_g is the number of grid points for the discretization. Usually the grid points are equally spaced on a logarithmic scale that covers the expected range of relaxation times to facilitate the

inversion problem.[12] The CONTIN method tries to solve the inversion problem in Eq. 6 by finding the constrained regularized solution $P(\tau_i)$ satisfying:

$$\sum_{j=1}^{N} w_j[\widetilde{g}_j^{(1)}(t_j) - \sum_{i=1}^{N_g} P(\tau_i)\exp(-t_j/\tau_i)]^2 + regularizor = minimum \tag{7}$$

where the $\widetilde{g}_j^{(1)}(t_j)$ are the N experimental values and w_j are optional weights on these data. Without the regularizor, the least-squares minimization yields an ill-conditioned problem and there are a very large number of possible solutions within the experimental noise. The regularizor adds further penalties on solutions that are either unphysical, i.e., with $P(\tau_i) < 0$, or have too much features, e.g., too large number of peaks given the experimental noise and the experimental time window.

The CONTIN software is very versatile and can be parametrized in many different ways depending on the experimental problem to be solved. Here we used it to solve Eq. 7 always with the following parametrization:

- the weights w_j were set uniformly to 1 to avoid possible artefacts linked with extra weight given to data at short delay times. In our case, this ensures that the fast decay mode is not enhanced by data weighting.

- a free baseline was always allowed.

- experimental data $\widetilde{g}_j^{(1)}(t_j)$ were fitted for delay times $0.5\mu s \leq t_j \leq 10s$.

- the window of relaxation times was set to $1\mu s \leq \tau \leq 1s$.

- the number of grid points was set to $N_g = 200$ to enhance the resolution and to allow a better fit and deconvolution of the different modes.

Prior to CONTIN analysis, the ICFs were checked to meet the following criteria: i) $\widetilde{g}^{(2)}(t) < 2$, ii) $\widetilde{g}^{(1)}(t > 10) \leq 0.01$, iii) $\Delta I_{tot}/I_{tot} < 0.6$, to prevent analysis of pathological ICFs, e.g., due to dust particles or intensity drifts. Here ΔI_{tot} is the standard deviation of the fluctuating total scattering intensity I_{tot} measured during the acquisition time. For measurements not meeting these criteria, only I_{tot} and ΔI_{tot} were kept as valid data reflecting the state of the solution.

2. Analysis of $P(\tau_i)$ and parameter definitions

The $P(\tau_i)$ resulting from CONTIN analysis was then fitted to a sum $S(\tau)$ of Gaussian functions on the logarithmic scale of the grid points:

$$S(\tau) = \sum_k a_k \exp(-\frac{(log(\tau) - log(\tau_k))^2}{\sigma_k^2}) \tag{8}$$

using a non-linear least-squares method implementing the Levenberg-Marquardt algorithm. The number k and the initial positions τ_k of the Gaussian peaks used in the fit were determined automatically by the second derivative algorithm, which was very efficient in this case because the CONTIN method produces naturally smooth $P(\tau_i)$ curves. If the fit completed successfully, the results were considered as satisfying if they met all the following criteria: i) $a_k > 0$, ii) number of iterations for fit convergence smaller than 30, iii) relative errors on a_k, τ_k, and σ_k smaller than 200%. Otherwise the results were discarded and not considered for further analysis.

For satisfying results we defined then for each peak the apparent hydrodynamic radius R_k following Eq. 1 in main text and the associated peak area $A_k = \sqrt{\pi} a_k \sigma_k$. We note that this peak area definition takes into account that $P(\tau_i)$ is already a discretization on a logarithmic scale of the normalized distribution of relaxation times $p(\tau)$. It ensures that A_k is proportional to the relative contribution I_k of decay mode k to the total scattering intensity I_{tot}. Thus:

$$\widetilde{g}^{(1)}(0) = \sum_{i=1}^{N_g} P(\tau_i) = \sum_{k=1}^{N_p} A_k \tag{9}$$

$$I_k = \frac{A_k}{\sum A_k} I_{tot} \tag{10}$$

where N_p is the number of peaks. These definitions were used to split the total scattering intensity into the intensities contributed by each decay mode.

Relative errors on the parameters R_k, A_k and I_k were defined from the relative errors $\delta\tau_k$, δa_k,

$\delta\sigma_k$, and the correlation factor C_k between a_k and σ_k obtained in the non-linear fitting as:

$$\delta R_k = \delta\tau_k \tag{11}$$

$$\delta A_k = [(\delta a_k)^2 + (\delta\sigma_k)^2 + 2C_k\delta a_k\delta\sigma_k]^{1/2} \tag{12}$$

$$\delta I_k = \delta A_k + \frac{\sum A_k\delta A_k}{\sum A_k} + \frac{\Delta I_{tot}}{\sqrt{255}I_{tot}} \tag{13}$$

where the numerical factor $1/\sqrt{255}$ comes from the fact that we use the standard error on the time-averaged I_{tot} to compute the errors on the time-averaged I_k. When plotting I_{tot}, we use ΔI_{tot} as error bars to give an idea about the amplitude of time fluctuations in the scattering intensities. For all other intensity plots, we use error bars defined by Eq. 13.

Fig. S4 shows typical results obtained during the analysis. These consecutive measurements show how CONTIN output can depend on data noise. The fitting algorithm found (Fig. S5) two peaks in measurement 0027 and only one in measurement 0028, where the small features at $t \leq 0.5$ ms were skipped by the fit because they correspond to a too weak relative contribution. The small peak at $t \approx 0.1$ s was excluded from the fitting range because it is obviously not corresponding to any decay in the data. This contribution is however influencing $P(\tau_i)$ at smaller t.

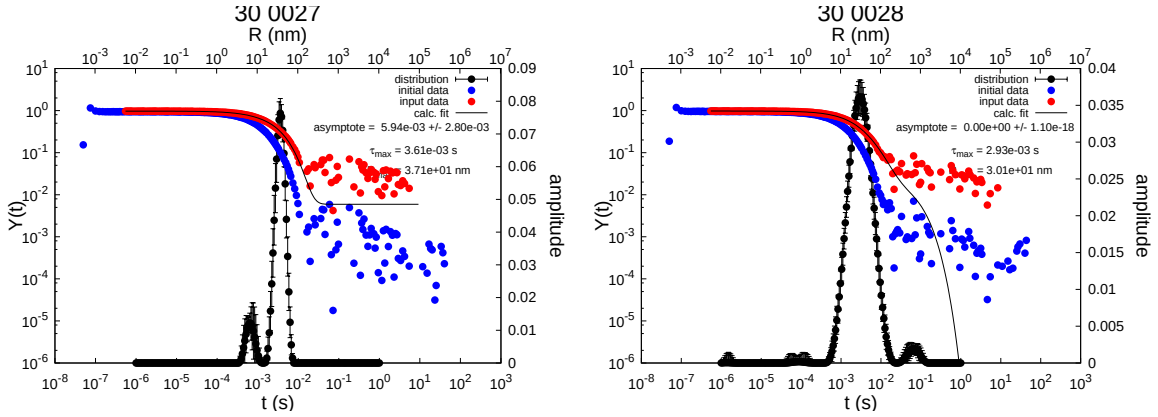

Figure S4: Two typical examples of CONTIN outputs. Sample P94 at 28°C, $\theta = 30°$. (•) $g^{(2)}(t) - 1$; (•) $\widetilde{g}^{(1)}(t)$; (•) $P(\tau_i)$. The continuous line shows the correlation function corresponding to $P(\tau_i)$.

3. Automated peak identification and sorting

Due to the experimental noise in the ICFs, the CONTIN analysis can produce spurious peaks in the $P(\tau_i)$ that should be discarded. To do this in an automated way, we first discarded peaks with

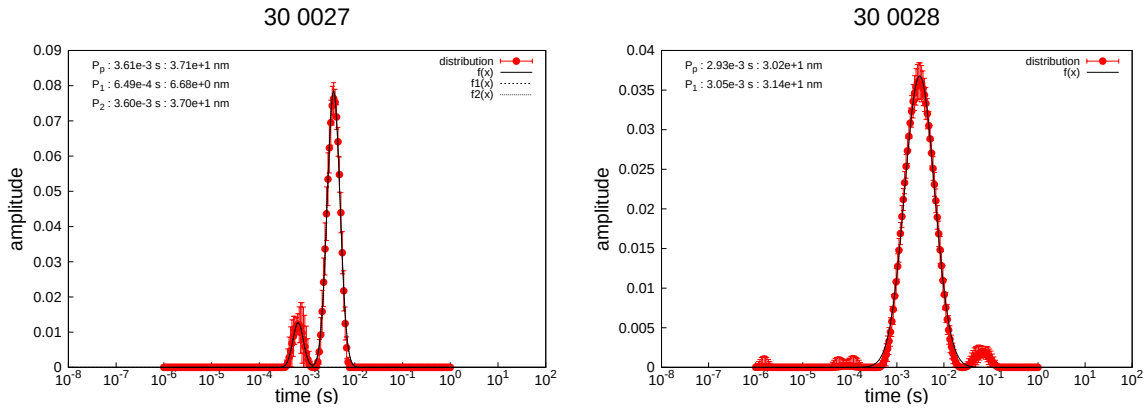

Figure S5: Fits of the CONTIN outputs $P(\tau_i)$ (•) by Gaussian peaks (lines). Same data as in Fig. S4.

$A_k/A_{max} < 0.005$, where A_{max} is the peak area of the major contribution in $P(\tau_i)$. The remaining contributions were then sorted by plotting an histogram of all R_k values as shown in Fig. S6.

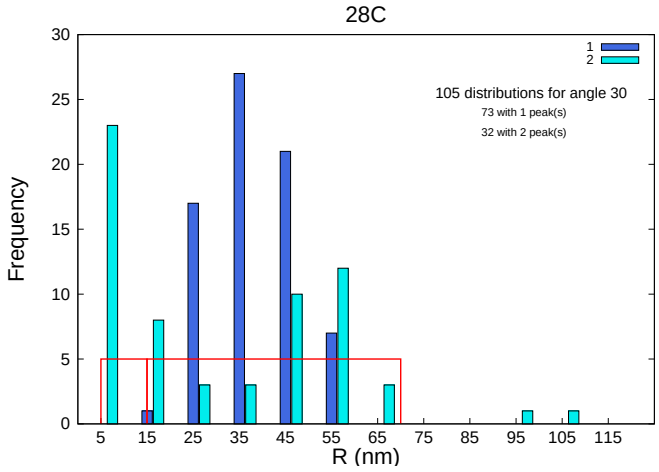

Figure S6: Histogram of the R_k values measured for P94 at $T = 28°C$ and $\theta = 30°$ in monomodal (•) or bimodal (•) $P(\tau_i)$. Bins are 10 nm wide and located at the center of the class, i.e., the bar at $R = 5$ nm corresponds to the frequencies for $0 < R \leq 10$. The red lines shows we defined two classes in this example: fast decay mode for $R \leq 15$ nm and slow decay mode for $15 < R \leq 70$. The two occurrences $R > 90$ nm were rejected as non-typical after a closer look at the data.

This typical example shows that, depending on the experimental noise, CONTIN either resolved two peaks with positions $R_k \approx 5$ nm and $R_{k+1} \approx 55$ nm or merged them in a broader peak at position $R_a \approx 35$ nm with $R_k < R_a < R_{k+1}$. Decision on the next step was achieved by comparing the relative frequencies of solutions with 1 or 2 peaks. The solutions with the largest frequency were usually considered as the most representative and we defined accordingly R intervals to assign the experimental R_k and I_k values to the fast or the slow components. In the present example,

although the solutions with a monomodal $P(\tau_i)$ outnumber the ones with a bimodal $P(\tau_i)$, we kept the bimodal description because it is consistent with the behavior at larger scattering angles.

When $P(\tau_i)$ with distinct peaks were in the minority, a merged contribution was calculated for them as:

$$I_a = I_k + I_{k+1} \tag{14}$$

$$I_a \delta I_a = I_k \delta I_k + I_{k+1} \delta I_{k+1} \tag{15}$$

$$R_a = \frac{R_k I_k + R_{k+1} I_{k+1}}{I_k + I_{k+1}} \tag{16}$$

$$(R_a \delta R_a)^2 = \frac{[(R_a - R_k)^2 + (R_k \delta R_k)^2] I_k + [(R_a - R_{k+1})^2 + (R_{k+1} \delta R_{k+1})^2] I_{k+1}}{I_k + I_{k+1}} \tag{17}$$

Depending on the respective weights I_k and I_{k+1}, R_a can be located in either the fast or the slow component class and the associated errors can be large, producing large fluctuations and error bars in the final plots. However we preferred to keep these values rather than to cherry-pick "good results". The amplitude of the fluctuations in the results helps one to appreciate how much confidence should be given to the existence of small decay modes at given temperature and scattering angle. The quality of mode splitting and its evolution with time can be further evaluated by plotting $I_k(R_k)$ with color coding of the decay modes (Fig. S7). In the present example, the definition of the two classes in Fig. S6 produces two distinct clouds of points, confirming that distinguishing two classes is meaningful. The elongated shape of these clouds is associated with the time evolution of $P(\tau_i)$. Here the ratio of intensities I_{slow}/I_{fast} is about 10 and the ratio of radii R_{slow}/R_{fast} about 5.

4. Other methods of analysis

In some cases, the ICFs were also fitted with either the modified cumulants[13]

$$g^{(2)}(t) = B + a_1 \exp(-2t/\bar{\tau})(1 + \frac{\mu_2}{2!}t^2 - \frac{\mu_3}{3!}t^3)^2 \tag{18}$$

or a forced bi-exponential fit

$$g^{(2)}(t) = B + [\sum_{k=1}^{2} a_k \exp(-t/\tau_k)]^2 \tag{19}$$

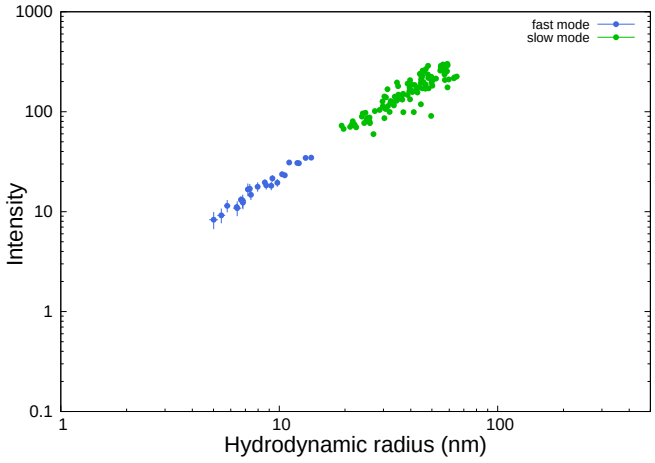

Figure S7: Plot of the intensity vs. the associated hydrodynamic radius for all the peaks in $P(\tau_i)$ obtained for sample P94 at $T = 28°C$, $\theta = 30°$.

If the fit completed successfully, the results were considered as satisfying if they met all the following criteria: i) $a_k > 0$, ii) number of iterations for fit convergence smaller than 150, iii) δa_k and $\delta\tau_k$ smaller than 50%. For the cumulants fit, it was also required that $\mu_2\bar{\tau}^2/2! - \mu_3\bar{\tau}^3/3! < 0.25$. Otherwise the results were discarded and not considered for further analysis.

For the bi-exponential fits, we defined then $A_k = a_k$ and $\delta A_k = \delta a_k$, and proceeded like above to sort the decay modes.

5. Comparison of the methods of analysis

When analyzing the decay of the ICFs during the kinetics of micellization or micelle growth, each method has its own advantages and drawbacks.

The modified cumulants approach is the simplest one and gives apparently good results, even in the case of a bimodal distribution of relaxation times if one decay mode is dominating the decay. The main drawback is that there is no way to check this condition is met. In the presence of a bimodal distribution of species, it gives an average AHR value strongly weighted by the micelles with the strongest contribution to I_{tot}. This average value is not simply related to the values obtained with either a CONTIN analysis or a bi-exponential fit and can shift progressively as the relative contributions of the decay modes to I_{tot} change. Moreover the information about minority decay modes is lost in the analysis. Therefore we used the modified cumulants analysis only when

CONTIN analysis indicated no doubt about the presence of a single decay mode in the ICF.

The CONTIN method has the advantage of giving hints for the presence of weak decay modes that are hardly detected by visual inspection of the ICFs. However CONTIN is really sensitive to the structure of data noise in the ICFs and small features can simply result from noise. Therefore they have to be confirmed by a large number of measurements and an adequate statistical analysis. By design CONTIN tries to smooth the distribution of relaxation times as long as the consistency with experimental data is kept. Thus it can be very difficult to distinguish two close decay modes with a relaxation time ratio smaller than 10, when their amplitude is not similar. In such cases, CONTIN tends to output a broader asymmetric peak.

Forced bi-exponential analysis is less sensitive to data noise than CONTIN and can resolve more easily close decay modes. However it will also distinguish two contributions in any single CONTIN peak with finite width. Therefore the choice of the number of components cannot be done blindly and has to be inferred from a preliminary CONTIN analysis. As the number of components N increases, N-exponentials analysis becomes more and more unsafe since it progressively yields an ill-conditioned problem where, due to the experimental noise, the least-squares minimization can be obtained for a very large set of solutions. CONTIN was precisely designed to address this problem. Finally a forced bi-exponential fit will not converge properly to the same solution as CONTIN when the latter produced a weak peak and a large broad peak. In this case the bi-exponential fit will always converge to two close modes describing the large broad peak and will neglect the small contribution. Fig. S8 compares the values of R_{slow} obtained with the three methods for one example. Although the trends and the orders of magnitude remain the same with the three analyses, the estimates for the times to reach equilibrium would differ with the three methods. Throughout this paper we preferred to use CONTIN analysis because it does not involve any assumption on the decay modes and the large number of measurements helped us to discriminate its possible artefacts. We used the other two methods only to confirm CONTIN results in the few experimental conditions where some ambiguity could remain.

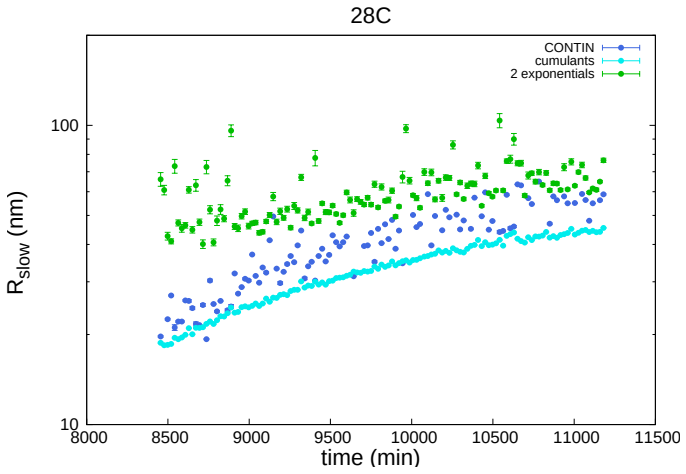

Figure S8: Time evolution of R_{slow} obtained with three different methods of analysis. (●) CONTIN; (●) modified cumulants; (●) 2-exponentials. Sample P94 at 28°C, $\theta = 30°$.

III. Crossover and polydispersity effects

We give here more technical details on measurement conditions that yield apparent hydrodynamic radius not reflecting the growing size of the polymer micelles.

1. Out of Guinier range

For a dilute solution of large polymers with radius of gyration $R_g \gg q^{-1}$ the classical result[14] is $\Gamma(q) \sim D_G R_g q^3$ where D_G is the translational diffusion coefficient of the chains. Since $D_G \sim 1/R_g$, $\Gamma(q)$ becomes independent of R_g in this regime,[14]

$$\Gamma(q) \approx 0.0788 \frac{k_B T}{\eta} q^3 \tag{20}$$

If unaware of this, one attempts to define an apparent hydrodynamic radius R_a from this decay rate, one gets a q-dependent quantity that is no longer related to the true dimension of the chains:

$$R_a(q) \approx 0.67 q^{-1} \tag{21}$$

Eqs. 20,21 are valid for a Zimm-like dynamics of the Brownian chains. For a Rouse-like behaviour, the exponent in Eq. 20 is 4.[14] Therefore, dynamic light scattering is said to probe the dynamics of internal relaxation modes of the large chains in the regime $qR_g \gg 1$.

2. Polydispersity

CONTIN solves for the $p(\tau)$ distribution in Eq. 6, which is weighted by the intensity scattered by the species. Therefore $p(\tau)$ depends also on the scattering vector q. As an example, consider a Schulz-Zimm distribution of homogeneous spheres described by:

$$F(R, R_n, z) = (\frac{z}{R_n})^z \frac{R^{z-1}}{\Gamma_a(z)} exp(-z\frac{R}{R_n}) \tag{22}$$

where R_n is the number averaged radius, $\Gamma_a(z)$ the Gamma function and $R_w = R_n(z+1)/z$ the weight averaged radius. The intensity scattered by a sphere with radius R is:

$$I(q, R) = R^6 (3\frac{sin(qR) - qRcos(qR)}{(qR)^3})^2 \tag{23}$$

and its weight in Eq.6 will be $F(R, R_n, z)I(q, R)$.[15]

Fig. S9 shows a plot of the distribution $F(R, R_n, z)$ for $R_n = 50$ nm and two values $z = 100$ and $z = 4$ and a plot of the apparent distribution measured at $q = 0.005$ nm^{-1} ($\theta \approx 20°$) and at $q = 0.025$ nm^{-1} ($\theta \approx 90°$) for $R_n = 50$ nm and $z = 4$.

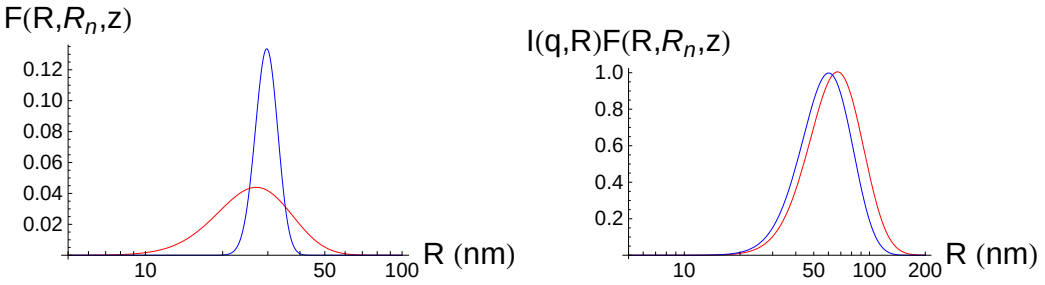

Figure S9: Left: Plot of the distribution $F(R, R_n, z)$ for $R_n = 30$ nm and two values of z, $z = 4$ (red) and $z = 100$ (blue); Right: Plot of the weighted apparent distribution measured at $q = 0.005$ nm^{-1} ($\theta \approx 20°$, red) and at $q = 0.025$ nm^{-1} ($\theta \approx 90°$, blue) for $R_n = 30$ nm and $z = 4$.

Clearly the apparent distributions are shifted to higher R values, as expected because of the R^6 weight, but also their position depends on the scattering angle. As a consequence, defining an apparent hydrodynamic radius for a rather polydisperse sample can yield a q-dependent quantity, even in the Guinier regime. The shift is here about 10% and increases as the fraction of chains having a size larger than q^{-1} increases. No noticeable shift is obtained in the case $z = 100$.

3. To semidilute range

Starting from a dilute solution of polymerizing units with concentration C, their average hydrodynamic radius R_h will progressively increase as the reaction proceeds. However as R_h becomes of the same order of magnitude as the mean distance between the chains, the polymers start to entangle and one enters the semidilute regime where the Brownian motion corresponds to the collective fluctuations of concentration of the temporary network formed by the entangled chains.[16] The corresponding collective diffusion coefficient is then related to the characteristic mesh size $\xi \sim C^{-3/4}$ of the entangled solution and no longer to the molecular dimensions of the entangled chains. During the polymerization (or the growth transition of polymer micelles as well), there will be a crossover from the dilute regime, where $D \sim 1/R_h$, to the semidilute regime, where $D \sim 1/\xi$ becomes a constant depending on the polymer concentration. Thus, there will be an apparent levelling off of the apparent hydrodynamic radius even if the growth is still going on.

IV. Specific results

1. Angular dependence of slow decay mode intensity for P84 at $T = 32, 33°\mathrm{C}$

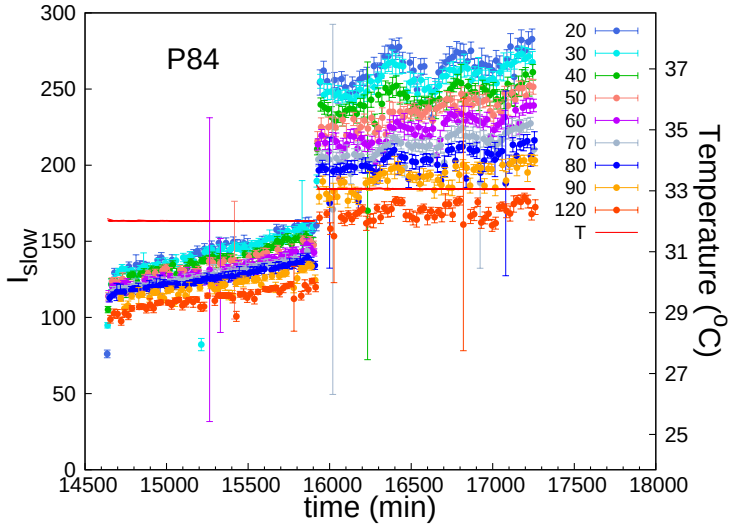

Figure S10: Time evolution of I_{slow} for all measured scattering angles. Sample P84 at $T = 32, 33°$.

2. Angular dependence of slow decay mode for P94 at $T = 29, 30°C$

In Fig. S11 it can be seen that the scattering intensity I_{slow} starts increasing rapidly at $t \approx 13000$ min for the larger angles. At about the same time, R_{slow} stops increasing at the smallest scattering angles. As a consequence, the angular dissymmetry is decreasing and the range of R_{slow} values measured at the different θ values shrinks. This behavior marks the crossover to the semidilute regime for the wormlike micelles. At $T = 30°$, the crossover is achieved, the further increase in I_{slow} is much smaller and R_{slow} becomes independent of θ (Fig. S12).

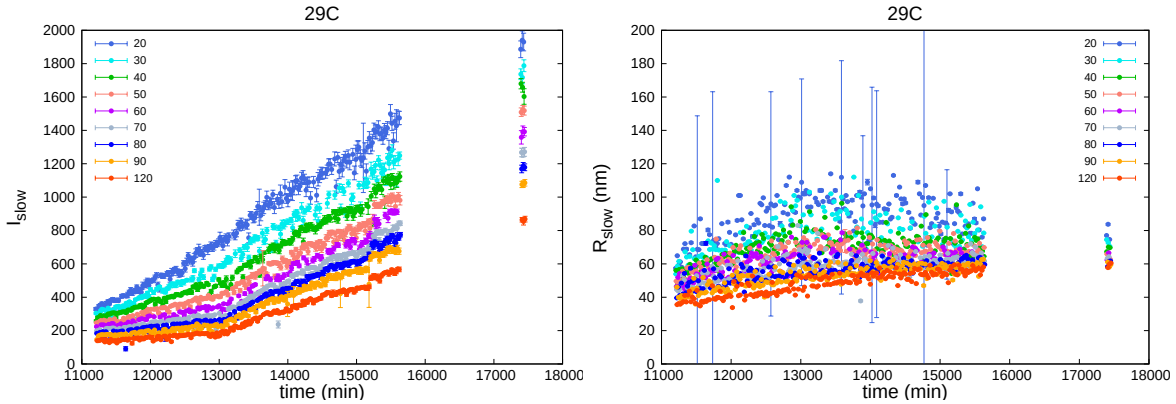

Figure S11: Time evolution of I_{slow} and R_{slow} for all measured scattering angles. Sample P94 at $T = 29°$. The time gap corresponds to unattended failure of the acquisition software.

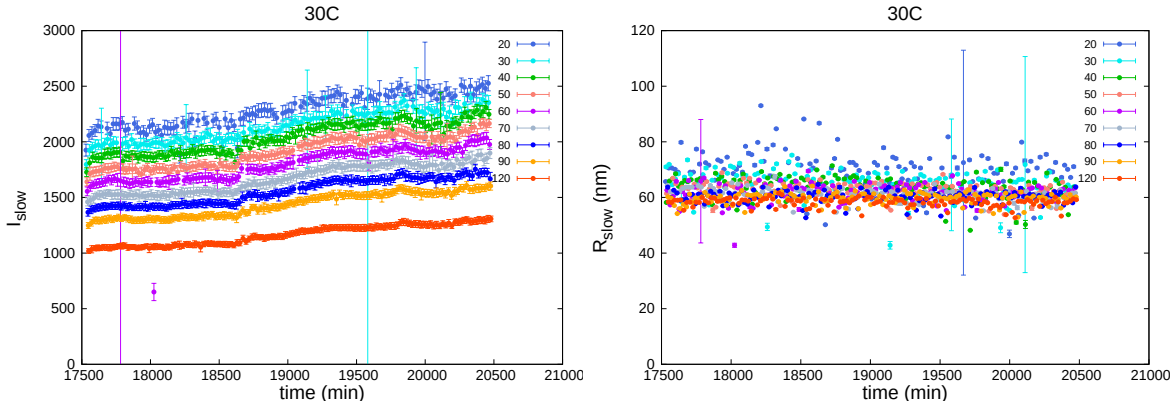

Figure S12: Time evolution of I_{slow} and R_{slow} for all measured scattering angles. Sample P94 at $T = 30°$.

3. Angular dependence of fast and slow modes for P104 at $T = 34°C$

Fig. S13 shows the time evolution of the angular dependence of the two decay modes for P104 sample at $T = 34°$. For the fast mode, a q-dependence starts to show up for the smallest scattering angles

in both the scattering intensity and the apparent hydrodynamic radius. For the slow mode, the intensity is plotted on a logarithmic scale to emphasize that it is increasing in time with no change in the q-dependence, i.e., at constant average radius of gyration. Values for the corresponding AHRs are strongly dependent on scattering angle and nearly independent of time within experimental accuracy.

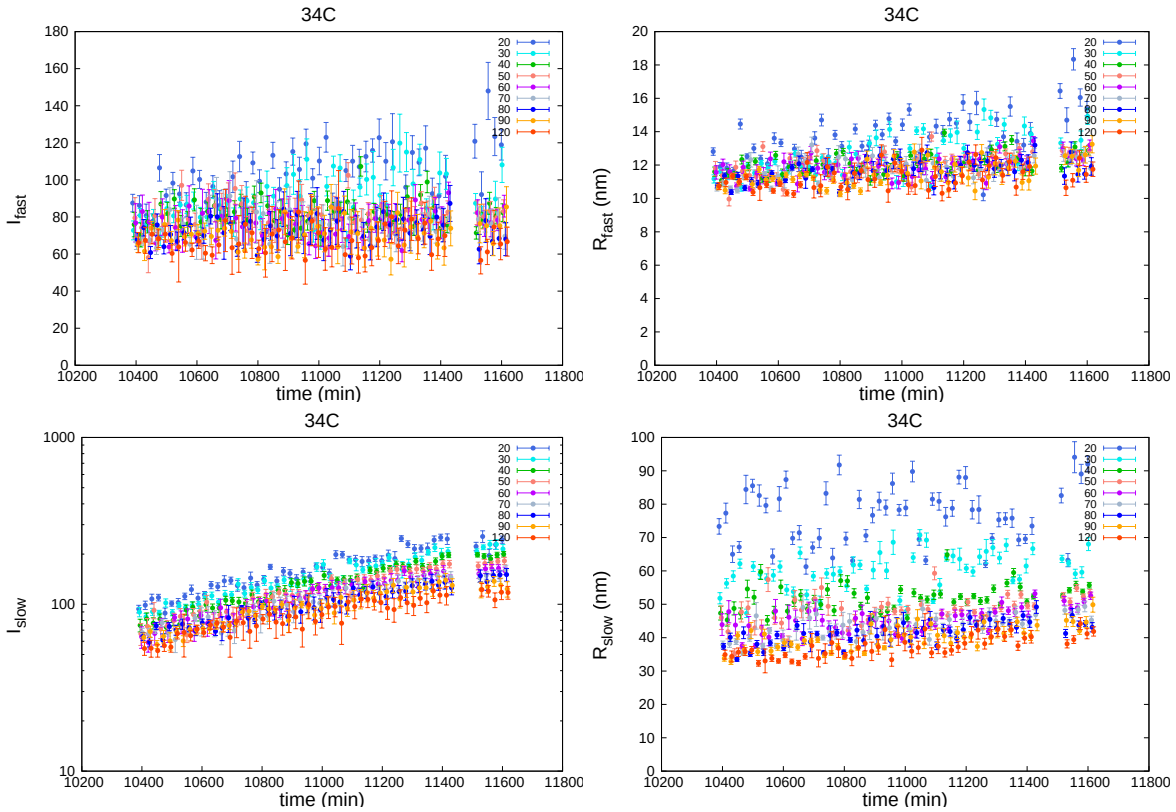

Figure S13: Time evolution of the angular dependence of the fast (above) and slow (below) decay modes for all measured scattering angles. Sample P104 at $T = 34°$.

References

(1) Zhou, Z.; Chu, B. Anomalous association behavior of an ethylene oxide/propylene oxide ABA block copolymer in water. *Macromolecules* **1987**, *20*, 3089–3091.

(2) Hvidt, S.; Joergensen, E. B.; Brown, W.; Schillen, K. Micellization and Gelation of Aqueous Solutions of a Triblock Copolymer Studied by Rheological Techniques and Scanning Calorimetry. *J. Phys. Chem.* **1994**, *98*, 12320–12328.

(3) Kositza, M. J.; Bohne, C.; Alexandridis, P.; Hatton, T. A.; Holzwarth, J. F. Micellization Dynamics and Impurity Solubilization of the Block-Copolymer L64 in an Aqueous Solution. *Langmuir* **1999**, *15*, 322–325.

(4) Fernandez, V. V. A.; Soltero, J. F. A.; Puig, J. E.; Rharbi, Y. Temporal Evolution of the Size Distribution during Exchange Kinetics of Pluronic P103 at Low Temperatures. *J. Phys. Chem. B* **2009**, *113*, 3015–3023.

(5) Holzgrabe, U.; Diehl, B. W.; Wawer, I. NMR spectroscopy in pharmacy. *J. Pharm. Biomed. Anal.* **1998**, *17*, 557 – 616.

(6) Izunobi, J. U.; Higginbotham, C. L. Polymer Molecular Weight Analysis by 1H NMR Spectroscopy. *J. Chem. Educ.* **2011**, *88*, 1098–1104.

(7) Postma, A.; Davis, T. P.; Donovan, A. R.; Li, G.; Moad, G.; Mulder, R.; O'Shea, M. S. A simple method for determining protic end-groups of synthetic polymers by 1H NMR spectroscopy. *Polymer* **2006**, *47*, 1899 – 1911.

(8) Foster, B.; Cosgrove, T.; Hammouda, B. Pluronic Triblock Copolymer Systems and Their Interactions with Ibuprofen. *Langmuir* **2009**, *25*, 6760–6766.

(9) Echavarri Franco, I.; Lorchat, P.; Lamps, J.-P.; Schmutz, M.; Schröder, A.; Catala, J.-M.; Combet, J.; Schosseler, F. From Chain Collapse to New Structures: Spectroscopic Properties of Poly(3-thiophene acetic acid) upon Binding by Alkyl Trimethylammonium Bromide Surfactants. *Langmuir* **2012**, *28*, 4815–4828.

(10) Berne, B. J.; Pecora, R. Dynamic Light Scattering with Applications to Chemistry, Biology, and Physics. **1976**, Wiley Interscience, New York.

(11) (a) Provencher, S. W. A constrained regularization method for inverting data represented by linear algebraic or integral equations. *Comput. Phys. Commun.* **1982**, *27*, 213 – 227; (b) Provencher, S. W. CONTIN: A general purpose constrained regularization program for inverting noisy linear algebraic and integral equations. *Comput. Phys. Commun.* **1982**, *27*, 229 – 242.

(12) Ostrowsky, N.; Sornette, D.; Parker, P.; Pike, E. Exponential Sampling Method for Light Scattering Polydispersity Analysis. *Optica Acta* **1981**, *28*, 1059–1070.

(13) Frisken, B. J. Revisiting the Method of Cumulants for the Analysis of Dynamic Light-Scattering Data. *Appl. Opt.* **2001**, *40*, 4087–4091.

(14) Doi, M.; Edwards, S. F. The Theory of Polymer Dynamics. **1986**, Oxford University Press, Oxford.

(15) Kotlarchyk, M.; Stephens, R. B.; Huang, J. S. Study of Schultz distribution to model polydispersity of microemulsion droplets. *J. Phys. Chem.* **1988**, *92*, 1533–1538.

(16) de Gennes, P. G. Scaling Concepts in Polymer Physics. **1979**, Ithaca Press, New York.